Interannual Variability of Stratospheric Final Warming in the Southern Hemisphere and Its Tropospheric Origin

SOICHIRO HIRANO,[a] MASASHI KOHMA,[b] AND KAORU SATO[b]

[a] *Department of Physics and Earth Sciences, University of the Ryukyus, Okinawa, Japan*
[b] *Department of Earth and Planetary Science, The University of Tokyo, Tokyo, Japan*

(Manuscript received 7 December 2020, in final form 5 April 2021)

ABSTRACT: The relation between interannual variability of stratospheric final warming (SFW) and tropospheric circulation in the Southern Hemisphere (SH) is explored using reanalysis data and a linear barotropic model. The analysis is focused on quasi-stationary waves with zonal wavenumber 1 ($s = 1$ QSWs; s is zonal wavenumber), which are the dominant component of the SH extratropical planetary waves. First, interannual variability of SFW is investigated in terms of amplitudes of stratospheric and tropospheric $s = 1$ QSWs, and wave transmission properties of the mean flow from the late austral winter to spring. Upward Eliassen–Palm flux due to $s = 1$ QSWs is larger from the stratosphere down to the middle troposphere in early-SFW years than late-SFW years. More favorable conditions for propagation of $s = 1$ stationary waves into the stratosphere are identified in early-SFW years. These results indicate that the amplification of tropospheric $s = 1$ QSWs and the favorable conditions for their propagation into the stratosphere lead to the amplification of stratospheric $s = 1$ QSWs and hence earlier SFWs. Next, numerical calculations using a linear barotropic model are performed to explore how tropospheric $s = 1$ QSWs at high latitudes amplifies in early-SFW years. By using tropical Rossby wave source and horizontal winds in the reanalysis data as a source and background field, respectively, differences in $s = 1$ steady responses between early- and late-SFWs are examined at high latitudes. It is suggested that the larger amplitudes of tropospheric $s = 1$ QSWs in early-SFW years are attributed to differences in wave propagation characteristics associated with structure of the midlatitude jets in austral spring.

KEYWORDS: Atmosphere; Stationary waves; Stratospheric circulation

1. Introduction

In the polar stratosphere, winter terminates with breakdown of the polar vortex called stratospheric final warming (SFW). During SFWs, the polar vortex decays and its center moves away from the pole. On the other hand, an anticyclone called the Australian high in the Southern Hemisphere (SH) develops to the south of Australia and moves to the South Pole (Harvey et al. 2002; Hirano et al. 2016). SFWs can impact tropospheric circulation (Sun and Robinson 2009; Sun et al. 2011; Byrne and Shepherd 2018; Lim et al. 2018; Butler and Domeisen 2021). Black and McDaniel (2007) found that geopotential height (GPH) anomalies from their climatology in the lower troposphere have characteristic longitudinal structure that exhibits much more asymmetry than the southern annular mode pattern at early and late stages of SFWs in the SH.

In the SH, the timing of SFW is later in the late 1990s than the late 1970s primarily because of stratospheric ozone loss (Waugh et al. 1999; Zhou et al. 2000; Karpetchko et al. 2005; Langematz and Kunze 2006; Black and McDaniel 2007; Haigh and Roscoe 2009). After around 2000, however, ozone concentration recovered gradually (Newman et al. 2006; Yang et al. 2008; Salby et al. 2012; Wilcox and Charlton-Perez 2013), and there is a slightly negative or almost no trend in the timing of SFW (Hirano et al. 2016). In addition to these trends, interannual variability of the timing of SFW associated with that of wave activity is observed in the variation of the timing of SFW (Hio and Yoden 2005; Hirano et al. 2016). Hirano et al. (2016) showed that the timing of SFW is significantly related with polar temperature and the vertical component of the Eliassen–Palm (EP) flux in the lower stratosphere during the austral spring. Furthermore, using a formula of three-dimensional residual mean flow (Kinoshita and Sato 2013), they revealed zonally asymmetric structure of adiabatic warming due to the residual mean flow.

In the SH upper troposphere, quasi-stationary waves with zonal wavenumber 1 ($s = 1$ QSWs; s is zonal wavenumber) have the largest amplitudes of planetary stationary waves in the extratropics (Turner et al. 2017). Quintanar and Mechoso (1995b) indicated using model simulations that tropospheric $s = 1$ QSWs at southern high latitudes are predominantly generated at low latitudes in the austral spring. Inatsu and Hoskins (2004) suggested that zonal asymmetries in tropical sea surface temperature (SST) contribute to the formation of wintertime extratropical stationary waves in the SH. On interannual time scales, previous studies pointed out that tropical SST variability can influence the polar stratospheric wave activity and temperature in both hemispheres. In particular, the influence of the canonical El Niño–Southern Oscillation (ENSO) and central Pacific ENSO, when eastern and central Pacific SST anomalies, respectively, are observed,

Denotes content that is immediately available upon publication as open access.

Corresponding author: Soichiro Hirano, soichiro@sci.u-ryukyu.ac.jp

DOI: 10.1175/JCLI-D-20-0945.1

has been investigated (Domeisen et al. 2019). In the SH, Hurwitz et al. (2011) compared responses of stratospheric temperature to the two types of ENSO during the austral spring and showed that polar temperature in the lower stratosphere is higher during the central Pacific El Niño, while the canonical El Niño does not significantly impact the stratospheric temperature. On the other hand, Lin et al. (2012) found that enhanced (suppressed) stratospheric planetary-wave activity is associated with the canonical La Niña–like (El Niño–like) and the central Pacific El Niño–like (La Niña–like) SST patterns. Moreover, previous studies dealing with stratospheric responses to tropical SST found Rossby wave train–like features propagating from lower to higher latitudes (Hurwitz et al. 2011, 2013; Lin et al. 2012; Yuan et al. 2018; Domeisen et al. 2019). However, detailed tropospheric conditions leading to earlier SFWs are still not elucidated well. Previous studies did not show the influence of the Rossby wave source (RWS; Sardeshmukh and Hoskins 1988) in the tropics and the midlatitude jets through which Rossby waves propagate in the troposphere on the timing of SFW.

In this study, the relation between the timing of SFW and tropospheric circulation is examined in detail. The analysis is focused on $s = 1$ QSWs. Their amplitudes are the largest of SH extratropical planetary waves in both the stratosphere and troposphere and attain a maximum in the austral spring (Randel 1988; Quintanar and Mechoso 1995a; Turner et al. 2017). It is confirmed that the main source of tropospheric $s = 1$ QSWs is at low latitudes in the austral spring (Quintanar and Mechoso 1995b). Thus, to clarify the influence of tropical RWS and midlatitude jets on the amplitudes of tropospheric $s = 1$ QSWs at high latitudes, remote $s = 1$ responses to the tropical RWS and the background flow are examined using a linear barotropic model. The linear barotropic model has been confirmed qualitatively to well reproduce steady extratropical responses to tropical heating in the literature (Hoskins and Ambrizzi 1993; Ambrizzi et al. 1995; Ting 1996; Ambrizzi and Hoskins 1997; Watanabe 2004). It should be noted that the strongest teleconnection between the tropics and southern high latitudes in the upper troposphere is observed during the austral spring (Jin and Kirtman 2009, 2010; Schneider et al. 2012; Yuan et al. 2018).

The following section describes data and methods used in this study. Section 3 focuses on extratropical $s = 1$ QSWs in both the stratosphere and troposphere. Their amplitudes and contribution to momentum balance are examined. Wave transmission properties of the mean flow for $s = 1$ stationary waves are also investigated in section 3. Section 4 explores how the amplitudes of tropospheric $s = 1$ QSWs in the extratropics are modulated by tropical convective heating and the midlatitude background flow using a linear barotropic model. Discussions are made in section 5. Section 6 gives concluding remarks.

2. Data and methods

This study uses 3-hourly three-dimensional wind, GPH, and temperature from the Modern-Era Retrospective Analysis for Research and Applications, version 2 (MERRA-2; Gelaro et al. 2017), covering the period of 38 years (1980–2017). The data are provided for 42 pressure levels from 1000 to 0.1 hPa with a horizontal interval of 1.25°.

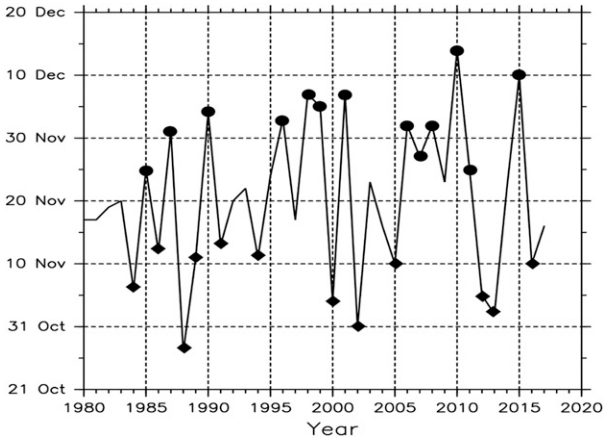

FIG. 1. Time series of SFW date at 10 hPa in the SH. Diamonds and circles denote early- and late-SFW years, respectively.

SFW dates are defined as the date when a 5-day running-mean zonal-mean zonal wind at 60°S and 10 hPa becomes easterly and the easterly lasts until the subsequent autumn (Eyring et al. 2006; Butchart et al. 2011; McLandress et al. 2012). A time series of the SFW date is shown in Fig. 1. The SFW dates range from 27 October (in 1988) to 14 December (in 2010) with a mean date of 20 November. Apparently, there are a positive trend from 1980 to around 2000 and an almost no or slightly negative trend after around 2000. Interannual variability of SFW date is probably comparable with the positive trend from 1980 to around 2000 and appears to overshadow the climate trend after around 2000. These characteristics are consistent with Hirano et al.'s (2016) results.

SFWs are classified into three groups according to their timing so that each group has an almost equal number of years (Hirano et al. 2016): early (27 October–13 November; 1984, 1986, 1988, 1989, 1991, 1994, 2000, 2002, 2005, 2012, 2013, and 2016), intermediate (16–24 November; 1980–83, 1992, 1993, 1995, 1997, 2003, 2004, 2009, 2014, and 2017), and late (25 November–14 December; 1985, 1987, 1990, 1996, 1998, 1999, 2001, 2006–08, 2010, 2011, and 2015) SFW groups. The early- and late-SFW years are denoted by diamonds and circles, respectively, in Fig. 1. Differences between the early- and late-SFW groups are examined to clarify how interannual variability of SFW date is related to stratospheric and tropospheric circulation in the austral spring. Note that the interannual variability of SFW date, rather than its trends, is expected to be reflected in the differences between early- and late-SFW years. This is because the influence of the climate trends on the variation of SFW date is probably smaller than the interannual variability and this results in the relatively unbiased distribution of early- and late-SFW years throughout the period analyzed in this study (Fig. 1; Hirano et al. 2016).

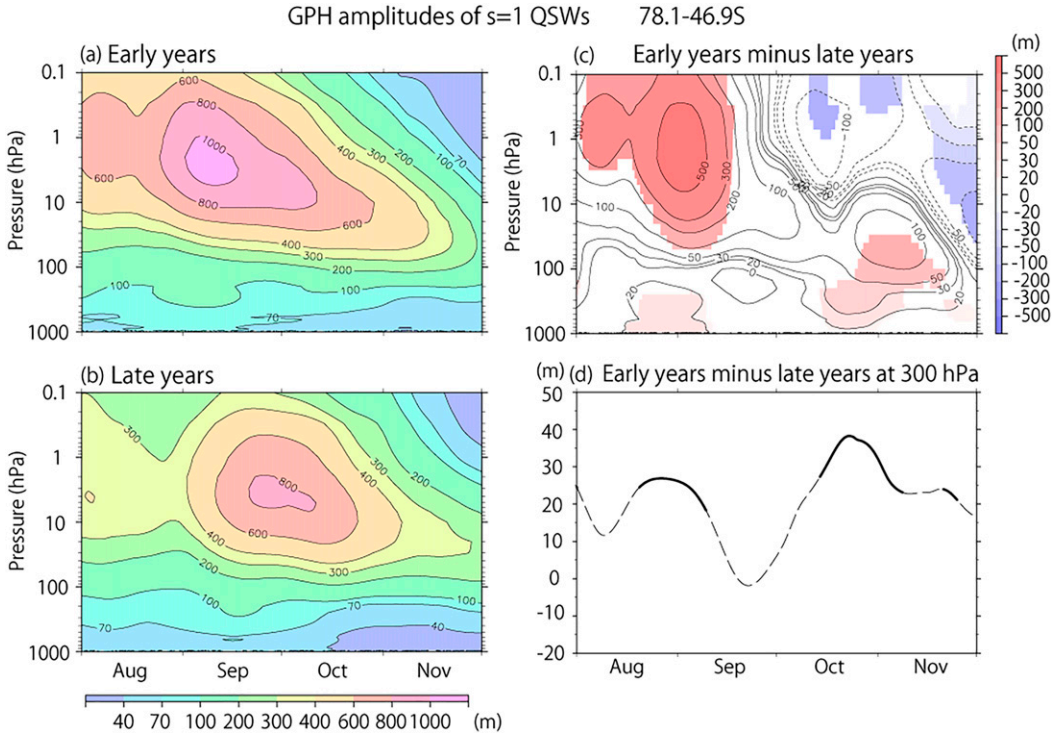

FIG. 2. Time evolution of (a) early- and (b) late-SFW composites of GPH amplitudes of $s = 1$ QSWs averaged over 78.125°–46.875°S. Contours representing 40, 70, 100, 200, 300, 400, 600, 800, and 1000 m are drawn. (c) Time evolution of an early-minus-late SFW composite of GPH amplitudes of $s = 1$ QSWs. Contours representing 0, ±20, ±30, ±50, ±100, ±200, ±300, and ±500 m are drawn. Only areas with the 95% confidence level for a two-sided t test are colored. (d) As in (c), but for 300 hPa. Bold solid curves indicate statistical significance at the 95% confidence levels for a two-sided t test.

3. The roles of stratospheric and tropospheric $s = 1$ QSWs in interannual variability of SFW date

a. Amplitudes of $s = 1$ QSWs

The relation of interannual variability of SFW date with stratospheric and tropospheric wave activity is examined in this subsection. Amplitudes of $s = 1$ QSWs are the largest of extratropical planetary waves in the SH stratosphere and attain a maximum in the austral spring (Randel 1988; Quintanar and Mechoso 1995a). Thus, the analysis is focused on the amplitudes of $s = 1$ QSWs, which are defined herein as the 30-day low-pass filtered components with zonal wavenumber 1 (Randel 1988; Harvey et al. 2002). Early- and late-SFW composites for GPH amplitudes of $s = 1$ QSWs averaged over 78.125°–46.875°S are shown in Figs. 2a and 2b, respectively. The latitudinal range for the averaging corresponds to the full width at half maximum of the wave amplitudes at 10 hPa in September–October. Amplitudes of stratospheric $s = 1$ QSWs attain their maximum in September–October, although the timing of the maximum is earlier and the maximum value is larger in early-SFW years than late-SFW years. To clarify differences between early- and late-SFW years, an early-minus-late SFW composite for $s = 1$ QSW amplitudes is displayed in Fig. 2c. In the stratosphere, a significant positive difference is observed above 50 hPa from mid-August to mid-September, and below 30 hPa from mid-October to mid-November. In both periods, significant positive differences are also observed at 300 hPa (Figs. 2c,d). These features indicate that the larger amplitudes of stratospheric $s = 1$ QSWs in early-SFW years than late-SFW years are related to tropospheric conditions. Moreover, a difference in amplitudes of $s = 1$ QSWs in the troposphere precedes a difference in the stratosphere from mid-October to mid-November (Fig. 2c). This suggests that the difference in stratospheric amplitudes of $s = 1$ QSWs originates in the troposphere. The origin of the differences in stratospheric wave amplitudes will be further examined using the EP flux in subsection 3b. The following analysis in this section is focused on the periods of 16 August to 15 September and 16 October to 15 November, which are hereafter referred to as periods 1 and 2, respectively.

Before showing the results for the analyses of $s = 1$ QSWs, we describe the seasonal evolution of the polar night jet (PNJ) from mid-August to mid-November in early- and late-SFW years. Zonal-mean zonal winds in early- and late-SFW years are shown in Figs. 3a–f for periods 1 and 2 as well as the time period between periods 1 and 2. Differences in zonal-mean zonal winds between early- and late-SFW years are also shown in Figs. 3g–i.

In period 1, the axis of the PNJ is located near 60°S below 0.3 hPa in early-SFW years (Fig. 3a). In late-SFW years, the

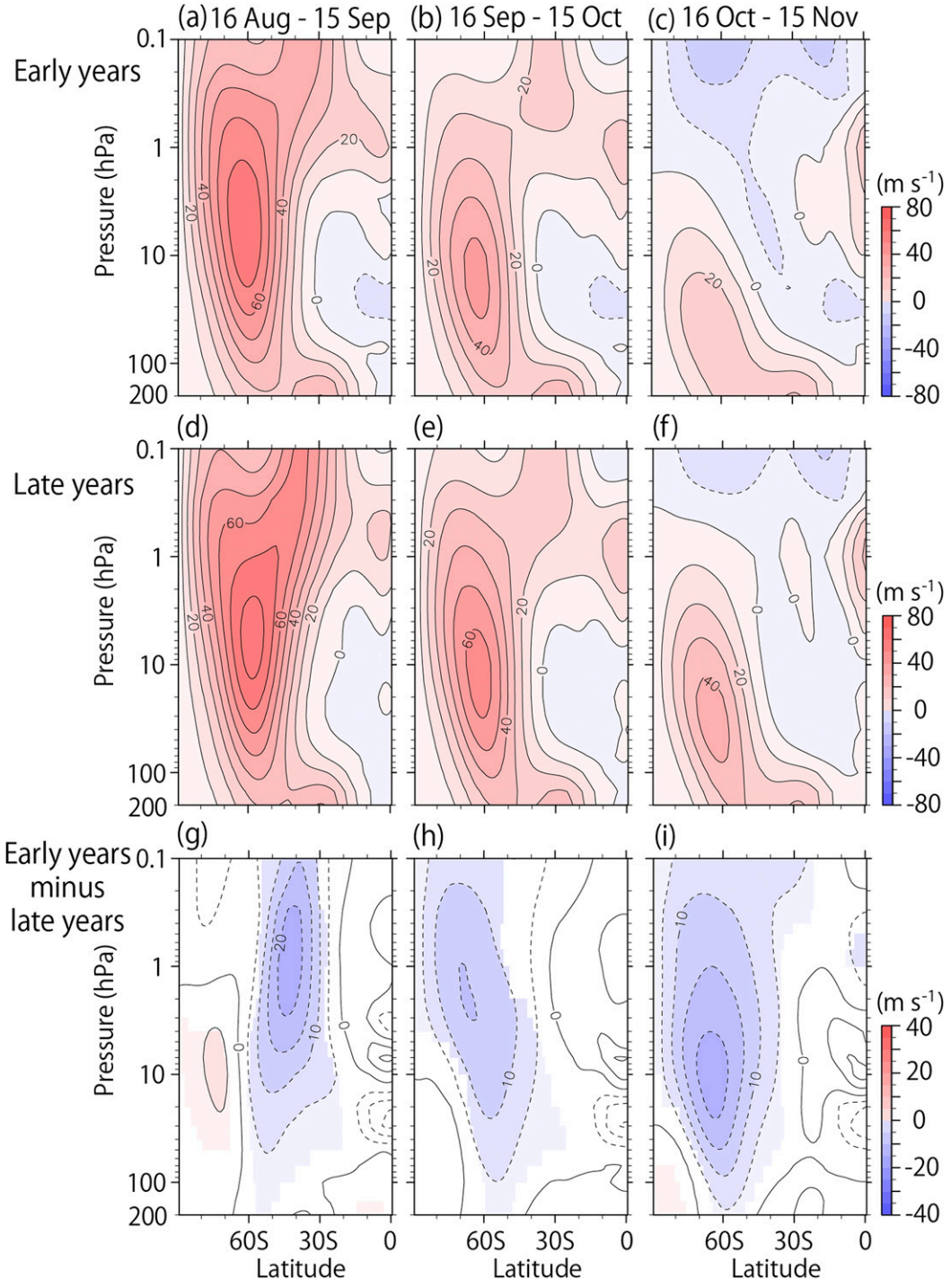

FIG. 3. Latitude–pressure cross sections of early-SFW composite of zonal-mean zonal winds during the time periods of (a) 16 Aug–15 Sep (period 1), (b) 16 Sep–15 Oct, and (c) 16 Oct–15 Nov (period 2). (d)–(f) As in (a)–(c), but for late-SFW composites. (g)–(i) As in (a)–(c), but for early-minus-late SFW composites. Only areas with the 95% confidence level for a two-sided *t* test are colored.

PNJ axis is located at lower latitudes at higher altitudes above 2 hPa (Fig. 3d). A large significant negative difference in zonal winds is observed in the latitudinal range of 60°–30°S above 50 hPa, that is, to the north of the PNJ core (Fig. 3g). These features indicate that the PNJ core migrates poleward earlier in early-SFW years than late-SFW years in period 1. From mid-September to mid-October and period 2, a negative difference in zonal winds is observed poleward of 40°S (Figs. 3h,i). The

magnitude of the negative difference in period 2 is larger than that from mid-September to mid-October, and comparable to that in period 1 (Figs. 3g–i).

b. *The relation between wave forcing due to stratospheric* s = *1 QSWs and zonal-mean zonal wind fields prior to SFWs*

To clarify the relation between wave forcing due to stratospheric $s = 1$ QSWs and zonal-mean zonal wind fields, differences in several terms of the zonal momentum equation between early- and late-SFW years are calculated in periods 1 and 2. The zonal momentum equation in the quasigeostrophic (QG) two-dimensional transformed Eulerian-mean (TEM) framework (Andrews and McIntyre 1976, 1978) is expressed as

$$\overline{u}_t - f_0\overline{v}^* = \frac{1}{\rho_0 a\cos\phi}\nabla\cdot\mathbf{F} + \overline{X}, \tag{1}$$

where ϕ is the latitude, t is time, ρ_0 is the basic density, f_0 is the Coriolis parameter at a given latitude, a is Earth's radius, $\overline{u}$ is the zonal-mean zonal wind, $\overline{v}^*$ is the meridional component of the residual mean flow, $\mathbf{F}$ is the EP flux, $\overline{X}$ is the zonal-mean zonal component of unspecified friction or other nonconservative mechanical forcings, and the subscripts refer to derivatives with respect to the given variable. The basic density ρ_0 is expressed as

$$\rho_0 = \rho_s e^{-z/H}, \tag{2}$$

where z is the height, H is the scale height, and ρ_s is standard reference density. The EP flux is represented as

$$\mathbf{F} = (F^{(\phi)}, F^{(z)}) = a\rho_0(\hat{F}^{(\phi)}, \hat{F}^{(z)}), \tag{3}$$

where

$$\hat{F}^{(\phi)} = -\overline{u'v'}\cos\phi \tag{4}$$

and

$$\hat{F}^{(z)} = f_0\frac{\overline{v'\theta'}}{\overline{\theta}_z}\cos\phi, \tag{5}$$

respectively, where u and v are the zonal and meridional components of wind velocity, respectively; θ is the potential temperature; and the bars and primes denote zonal means and deviations from the zonal means, respectively. The flux $(\hat{F}^{(\phi)}, \hat{F}^{(z)})$ is called the normalized EP flux in this study.

Early-minus-late SFW composites for several terms in Eq. (1) are shown in Fig. 4. The contribution of $s = 1$ QSWs is calculated for the normalized EP flux and divergence of the EP flux (Figs. 4c,f). The normalized EP fluxes shown in Figs. 4c and 4f are multiplied by $e^{-z/(2H)}$. Note that differences in the EP flux divergence due to waves with $s \geq 2$ are statistically insignificant in most of the region (not shown).

In period 1, a significant difference in upward EP flux due to $s = 1$ QSWs are observed below 0.3 hPa down to 500 hPa especially near 60°S, while there is a significant difference in northward EP flux near 10–0.3 hPa and 50°–30°S (Fig. 4c). The difference in upward EP flux indicates that the increased stratospheric $s = 1$ QSW activity originates in the troposphere. This is consistent with the simultaneous occurrence of positive differences in amplitudes of $s = 1$ QSWs above the middle stratosphere and in the troposphere in period 1 (Figs. 2c,d). A negative difference in the EP flux divergence due to $s = 1$ QSWs corresponds to a negative difference in the Coriolis torque near 3–0.3 hPa and 60°–30°S (Figs. 4b,c). This suggests that the increased deposition of negative momentum at midlatitudes near the stratopause advances poleward migration of the core of the PNJ in early-SFW years (Figs. 3a,d,g). Note that a negative difference in zonal wind tendency is observed near 10–0.4 hPa and 75°–50°S and does not correspond to the differences in the other two terms (Fig. 4a). Although differences in parameterized gravity wave drag as well as analysis increments may have a nontrivial effect on the seasonal evolution of the PNJ (e.g., McLandress et al. 2012), their magnitudes would be one order smaller than that of the difference in the EP flux divergence due to $s = 1$ QSWs.

In period 2, the analysis is focused on differences in the middle and lower stratosphere because the polar vortex already disappears in the upper stratosphere in early-SFW years. A significant difference in upward EP flux is seen near 80°–50°S below 20 hPa down to 500 hPa (Fig. 4f). This indicates that the difference in stratospheric activity of $s = 1$ QSWs comes from the troposphere and is consistent with the positive differences in amplitudes of lower stratospheric and tropospheric $s = 1$ QSWs in period 2, as in period 1 (Figs. 2c,d). A negative difference in the EP flux divergence due to $s = 1$ QSWs near 70–10 hPa corresponds to a negative difference in the Coriolis torque poleward of 25°S, and zonal wind tendency poleward of 60°S (Figs. 4d–f). The largest differences in the three terms are observed near 70°–60°S. The larger EP flux convergence likely leads to the weaker PNJ in the middle and lower stratosphere in early-SFW years than late-SFW years (Figs. 3c,f,i). Note that a positive difference in the Coriolis torque is observed near the stratopause. This is probably because westerlies are already replaced by easterlies in early-SFW years, while westerlies are still observed in late-SFW years near the stratopause (Figs. 3c,f).

These results suggest that the larger EP flux convergence in the stratosphere leads to earlier seasonal evolution of the PNJ in early-SFW years, namely the more advanced poleward shift of the core of the PNJ near the stratopause in period 1, and the weaker PNJ in the lower stratosphere in period 2. This is consistent with Hirano et al.'s (2016) result that SFW date is earlier for years with larger time integration of the vertical component of the EP flux in the lower stratosphere especially from the late winter to spring.

c. *Wave transmission properties of the mean flow for* s = *1 stationary waves*

To examine the role of wave transmission properties of the mean flow in the larger amplitudes of stratospheric $s = 1$ QSWs in early-SFW years than late-SFW years, the distribution of the refractive index squared (n^2) is compared between early- and late-SFW years. The refractive index squared for waves with phase speed c_p and zonal wavenumber s is expressed as

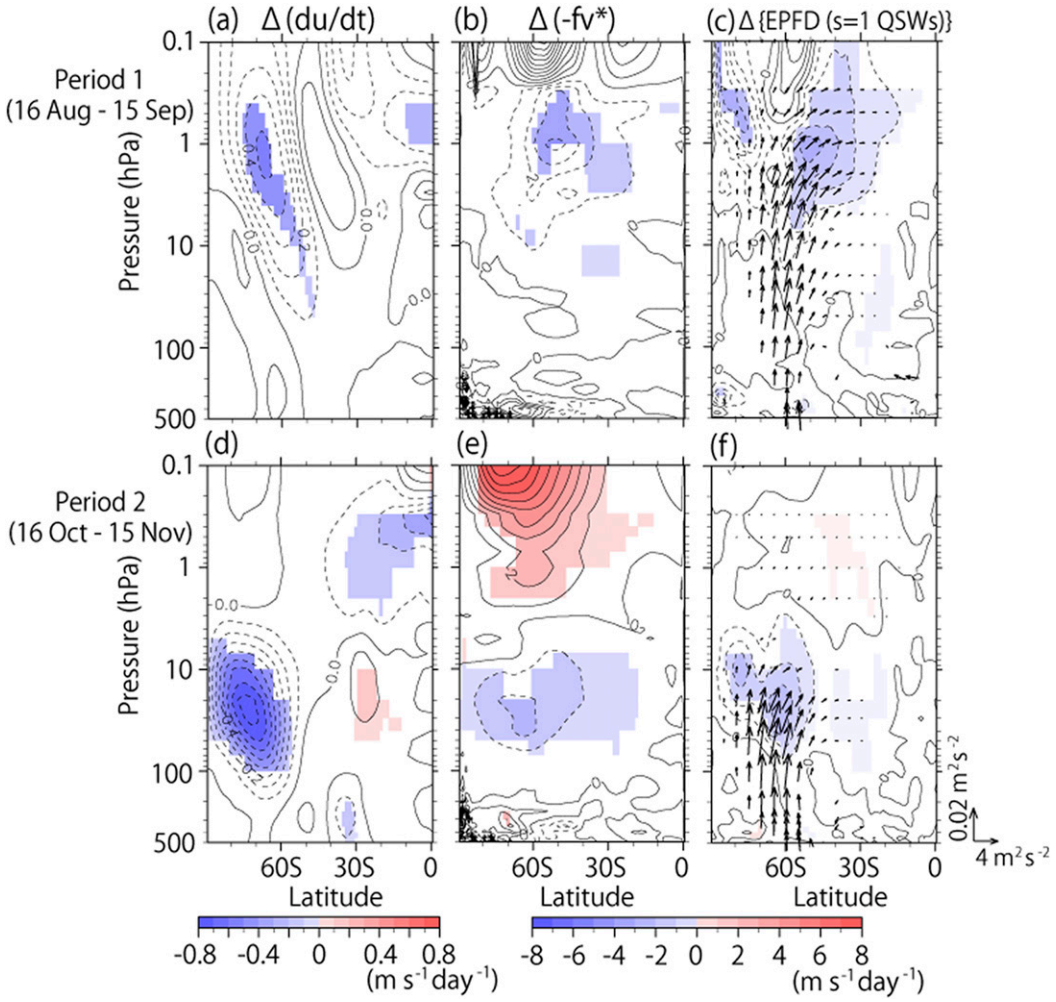

FIG. 4. Latitude–pressure cross sections of early-minus-late SFW composites of (a) tendency of the zonal-mean zonal wind, (b) $-f\overline{v}^*$, and (c) divergence of the EP flux (color) and the normalized EP flux (arrows) due to $s = 1$ QSWs in period 1. The normalized EP flux in (c) is multiplied by $e^{-z/(2H)}$. Contour intervals in (a) and in (b) and (c) are 0.1 and 1 m s^{-1} day^{-1}, respectively. Only areas with the 95% confidence level for a two-sided t test are colored. Arrows whose meridional or vertical component is significant at the 95% confidence level for a two-sided t test are drawn for the normalized EP flux. (d)–(f) As in (a)–(c), but for period 2. A reference arrow for the normalized EP flux is given on the right-hand side of (f).

$$n^2 = \frac{\overline{q}_\phi}{a(\overline{u} - c_p)} - \frac{s^2}{a^2\cos^2\phi} - \frac{f_0^2}{4N^2H^2}, \tag{6}$$

where

$$\frac{\overline{q}_\phi}{a} = \frac{2\Omega\cos\phi}{a} - \left[\frac{(\overline{u}\cos\phi)_\phi}{a^2\cos\phi}\right]_\phi - \frac{1}{\rho_0}\left(\frac{\rho_0 f_0^2}{N^2}\overline{u}_z\right)_z \tag{7}$$

is the meridional gradient of the zonal-mean QG potential vorticity; N is the buoyancy frequency; and Ω is the angular speed of rotation of Earth (Andrews et al. 1987).

Figure 5 shows n^2 multiplied by a^2 for $s = 1$ stationary waves in periods 1 and 2 for early- and late-SFW years. The EP flux due to $s = 1$ QSWs is also displayed in Fig. 5 to investigate the influence of the n^2 distribution on propagation of $s = 1$ QSWs. In period 1, the significant positive difference in $s = 1$ QSW amplitudes is observed in the upper stratosphere (Fig. 2c). Thus, differences in the distribution of n^2 are examined in the upper stratosphere in period 1. A surface of $n^2 = 0\,\text{m}^{-2}$ near 60°S is located near 0.5 hPa in early-SFW years, while that in late-SFW years is near 2 hPa (the horizontal red lines in Figs. 5a and 5b). A significant difference in upward EP flux is observed near 60°S between 2 and 0.5 hPa (Figs. 4c and 5a,b). These results indicate that the higher position of a surface of $n^2 = 0\,\text{m}^{-2}$ allows $s = 1$ stationary waves to propagate into higher altitudes in early-SFW years than late-SFW years.

In addition, to examine the roles of strength and structure of the PNJ in the formation of the n^2 distribution, differences in

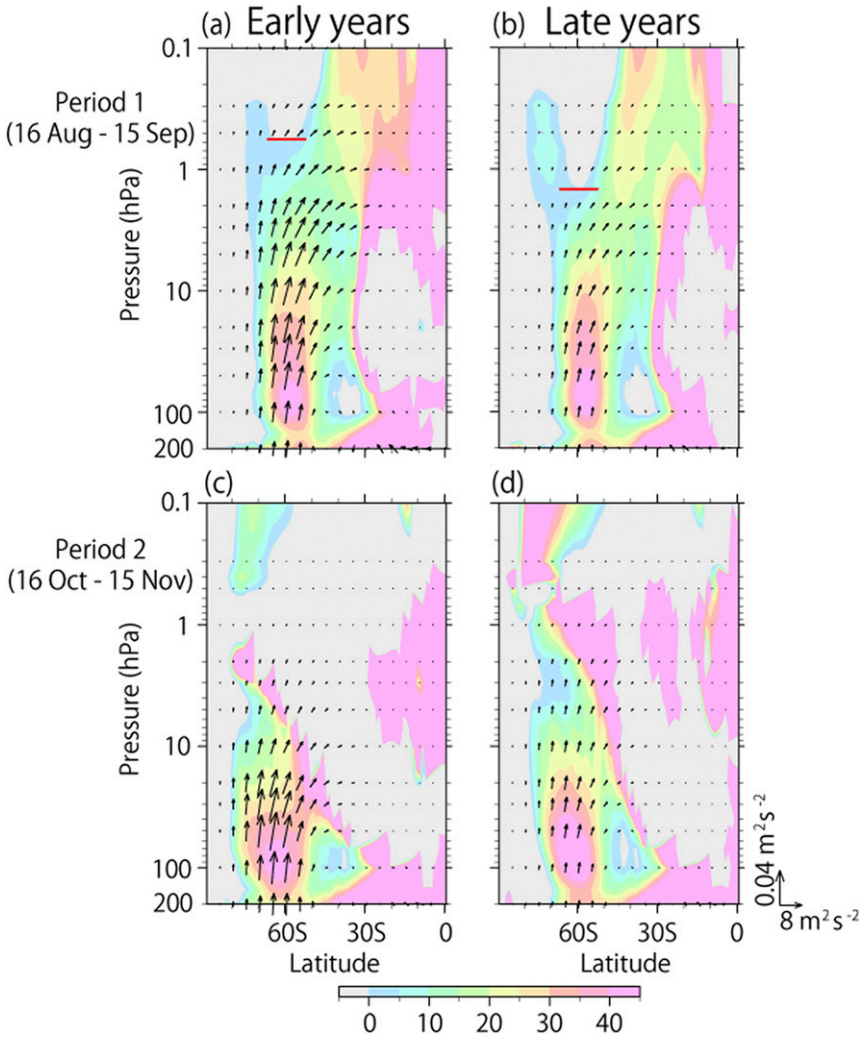

FIG. 5. Latitude–pressure cross sections of a^2n^2 for $s = 1$ stationary waves calculated from (a) early- and (b) late-SFW composites of the zonal-mean zonal wind and temperature in period 1. Areas with negative n^2 are colored gray. (c),(d) As in (a) and (b), but for period 2. Horizontal red lines in (a) and (b) denote the height of a surface of $n^2 = 0\,\mathrm{m}^{-2}$ near 60°S. The normalized EP flux due to $s = 1$ QSWs is also displayed. The normalized EP flux is multiplied by $e^{-z/(2H)}$. A reference arrow for the normalized EP flux is given on the right-hand side of (d).

the respective terms of the right-hand side of Eq. (7) multiplied by $a^2/\overline{u}$ between early- and late-SFW years are shown in Figs. 6a–c for period 1. The difference in the distribution of n^2 near 1 hPa is mainly attributable to a difference in the second term of the right-hand side of Eq. (7) multiplied by $a^2/\overline{u}$, that is, $-(1/\overline{u})[(\overline{u}\cos\phi)_\phi/\cos\phi]_\phi$ (Fig. 6b). The contributions of the first and third terms are minor (Figs. 6a,c). Note that a difference in the third term of Eq. (6) $-f^2/(4N^2H^2)$ is much smaller than those in the other three terms considered above (not shown).

Early- and late-SFW composites of $\overline{u}$ are also displayed in Figs. 6d and 6e to examine the relation between the distribution of n^2 and the structure of the PNJ. The PNJ axis is located near 60°S in early-SFW years, while it is located at lower latitudes at higher altitudes in late-SFW years, as mentioned in subsection 3a (Figs. 3a,d and 6d,e). The meridional curvature term $-(1/\overline{u})[(\overline{u}\cos\phi)_\phi/\cos\phi]_\phi$ is negative (positive) near the center (periphery) of the jet axis. A maximum of zonal wind is located near 60°S (50°S) near the stratopause in early-SFW (late SFW) years (Figs. 3a,d and 6d,e). A difference in zonal wind is small and statistically insignificant near 60°S and 1 hPa (Fig. 3g). The difference in the location of the zonal wind maximum creates the observed positive difference in $-(1/\overline{u})[(\overline{u}\cos\phi)_\phi/\cos\phi]_\phi$ near 60°S and 1 hPa. Therefore, it is suggested that the advanced poleward migration of the PNJ core is responsible for the higher position of a surface of $n^2 = 0\,\mathrm{m}^{-2}$ near the stratopause in early-SFW years.

In period 2, the positive difference in $s = 1$ QSW amplitude is observed from the lower stratosphere to the troposphere

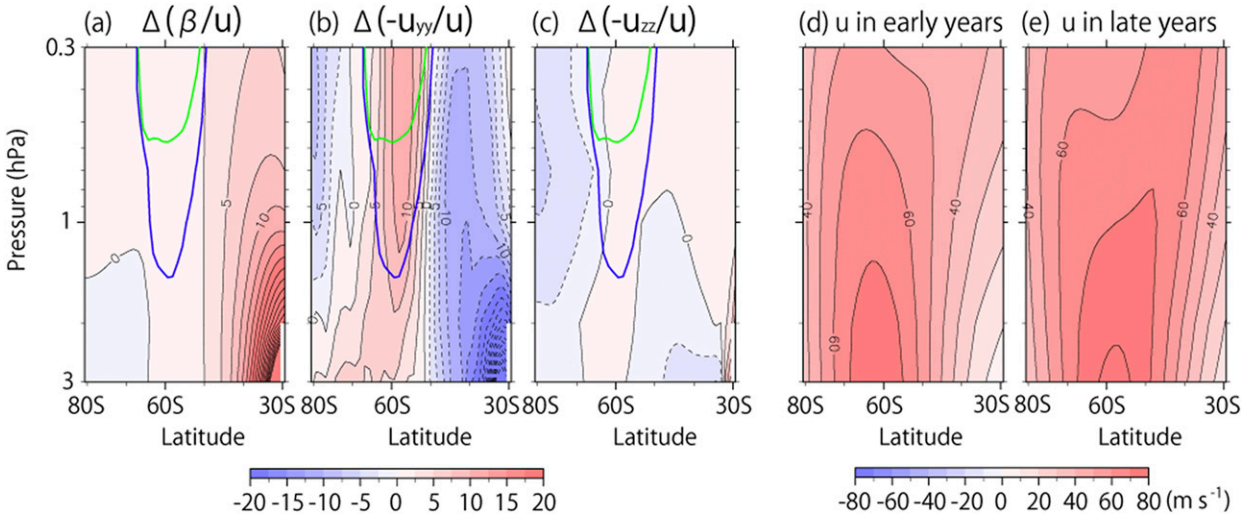

FIG. 6. Latitude–pressure cross sections of the (a) first, (b) second, and (c) third terms of Eq. (7) multiplied by $a^2/\bar{u}$ calculated from early-SFW composites of the zonal-mean zonal wind subtracted from those calculated from late-SFW composites in period 1. Thick green and blue curves indicate surfaces of $n^2 = 0\ \mathrm{m}^{-2}$ for early- and late-SFW years, respectively. Note that areas with the zonal-mean zonal winds of less than $5\ \mathrm{m\ s}^{-1}$ are not shown. (d) Early- and (e) late-SFW composites of the zonal-mean zonal wind in period 1; (d) and (e) are enlarged views of Figs. 3a and 3d near the stratopause, respectively.

(Fig. 2c). Upward EP flux is observed in the latitudinal range of 70°–55°S in the upper troposphere and lower stratosphere in both early- and late-SFW years (Figs. 5c,d). Although there is a slight difference in the distribution of n^2 in the lower stratosphere, a waveguide for vertical wave propagation, which is a region with large positive n^2 sandwiched by negative or small positive n^2 on its poleward and equatorward sides, is formed around 60°S in both early- and late-SFW years (Figs. 5c,d). These results suggest that the amplified lower stratospheric $s = 1$ QSWs in early-SFW years in period 2 are attributable to the amplified tropospheric waves rather than wave transmission properties of the mean flow in the upper troposphere and lower stratosphere.

4. Amplification of tropospheric $s = 1$ QSWs in period 2′

It is shown that amplitudes of tropospheric $s = 1$ QSWs are larger in the austral spring in early-SFW years than late-SFW years. Quintanar and Mechoso (1995b) explored the generation mechanism of tropospheric $s = 1$ QSWs at southern high latitudes in spring and suggested that they are predominantly generated at low latitudes. Moreover, Quintanar and Mechoso (1995b) pointed out several wave trains with equivalent barotropic structure propagating from lower latitudes. Hence, in this section, we explore how tropospheric $s = 1$ QSWs at southern high latitudes are amplified in early-SFW years in terms of wave sources in the tropics and horizontal propagation of waves.

Figure 7 shows scatter diagrams between amplitudes of $s = 1$ QSWs at 300 hPa and SFW date. In period 1, amplitudes of $s = 1$ QSWs are larger than the climatology for most early-SFW years (Fig. 7a). However, for nearly a half of late-SFW years, amplitudes of $s = 1$ QSWs are larger than the climatology (Fig. 7a). In contrast, in period 2, $s = 1$ QSW amplitudes are larger (smaller) than the climatology for early- (late-) SFW years with a few exceptions (Fig. 7b). Hence, we examine reasons for the larger amplitudes of tropospheric $s = 1$ QSWs in early-SFW years than late-SFW years in period 2. The analysis in this section is focused on the time period of 1 October–15 November, which is hereafter referred to as period 2′. This time period is chosen by extending period 2 forward by half a month, which roughly corresponds to the time that is necessary for wave trains to propagate from lower to higher latitudes (Li et al. 2015).

a. *Longitudinal structure of* s = *1 stationary waves in the upper troposphere at high latitudes*

The longitudinal phase structure and amplitudes of $s = 1$ stationary waves, and their differences between early- and late-SFW years are investigated at high latitudes in the upper troposphere. Early- and late-SFW composites of $s = 1$ GPH at 300 hPa, and their differences are displayed in Fig. 8. The longitudinal phase structure of $s = 1$ stationary waves at high latitudes in early-SFW years is similar to that in late-SFW years (Figs. 8a,b). A ridge of $s = 1$ stationary waves is located near the Amundsen Sea. As a result, a difference in $s = 1$ stationary waves primarily arises from a difference in their amplitudes (Fig. 8c). Note that $s = 1$ stationary waves have equivalent barotropic structure in the troposphere (not shown).

b. *The structure of jets and distribution of RWS in the upper troposphere*

Next, we examine extratropical mean flow and tropical wave sources, which may affect the amplitudes of $s = 1$ stationary waves at high latitudes. Zonal winds at 300 hPa in early- and late-SFW years, and their differences are displayed in Fig. 9. Double jet structure is seen especially in the longitudinal range

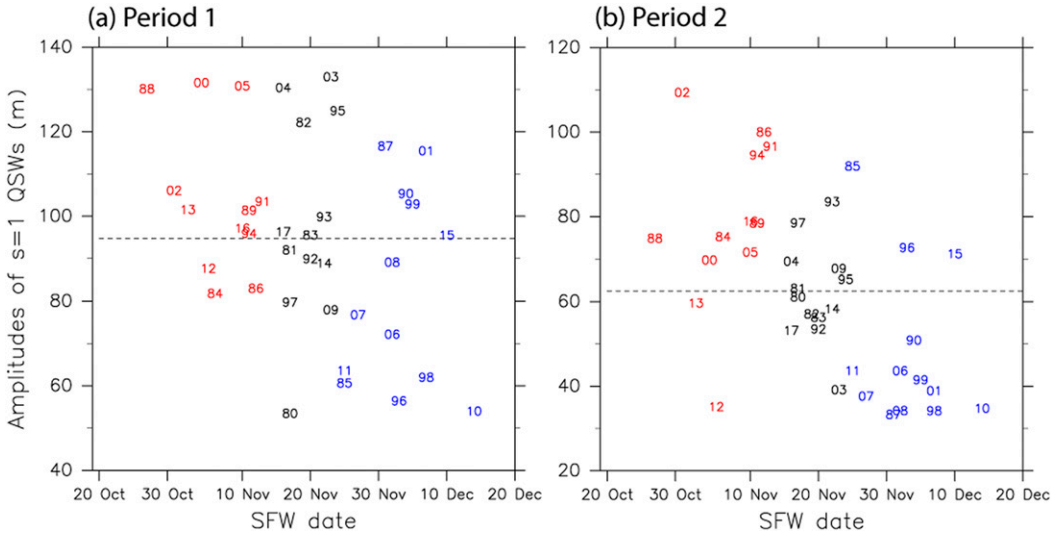

FIG. 7. Scatterplots of GPH amplitudes of $s = 1$ QSWs at 300 hPa averaged over 78.125°–46.875°S vs SFW date for (a) period 1 and (b) period 2. Individual years are indicated by numerals in the figures. Red, black, and blue numerals indicate early-, intermediate-, and late-SFW years, respectively. Dotted lines indicate the climatology of $s = 1$ QSW amplitudes.

of 90°E–150°W (Figs. 9a,b). These jets are hereafter called the subtropical jet and the polar jet. The polar jet is weaker especially near 90°E–90°W in early-SFW years, while significant positive differences in the subtropical jet are observed on its southward flank near 90°E–135°W (Fig. 9c).

RWS is expressed as

$$-\nabla \cdot (\zeta \mathbf{v}_\chi) = -\zeta \nabla \cdot \mathbf{v}_\chi - \mathbf{v}_\chi \nabla \zeta, \tag{8}$$

where ζ is the vertical component of the absolute vorticity, and $\mathbf{v}_\chi$ is the horizontal components of divergent wind (Sardeshmukh and Hoskins 1988). RWSs and the horizontal components of divergent wind at 300 hPa in early- and late-SFW years, and their differences are displayed in Fig. 10. Large RWS is observed poleward of 20°S and 20°N in early- and late-SFW years (Figs. 10a,b). Although large divergence associated with deep convection is concentrated in the tropics, RWS is small in the tropics. The first term on the right-hand side of Eq. (8) $-\zeta \nabla \cdot \mathbf{v}_\chi$ is small in the tropics because divergence is multiplied by absolute vorticity and the absolute value of absolute vorticity is smaller at lower latitudes. The largest value of $-\mathbf{v}_\chi \nabla \zeta$ is observed

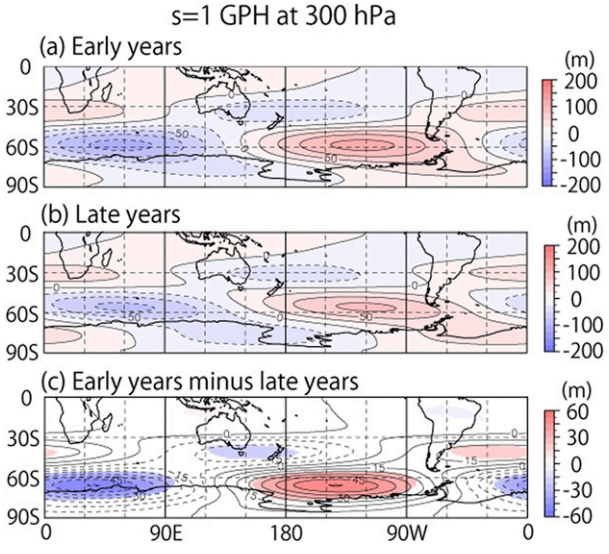

FIG. 8. (a) Early-, (b) late-, and (c) early-minus-late SFW composites of GPH with zonal wavenumber 1 at 300 hPa in period 2′. Only areas with the 95% confidence level for a two-sided t test are colored in (c).

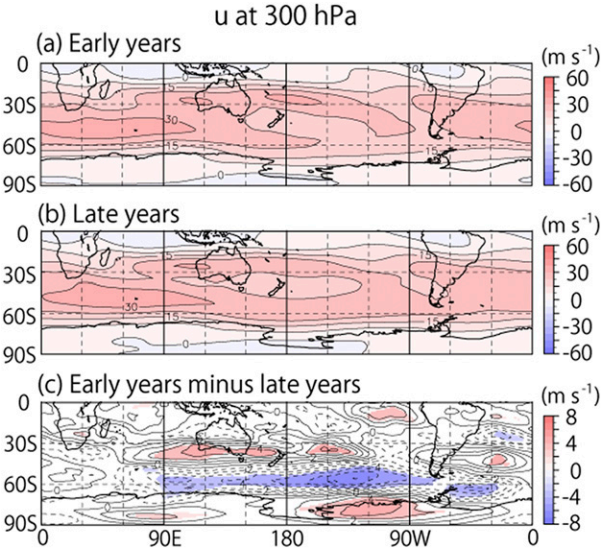

FIG. 9. As in Fig. 8, but for zonal wind at 300 hPa.

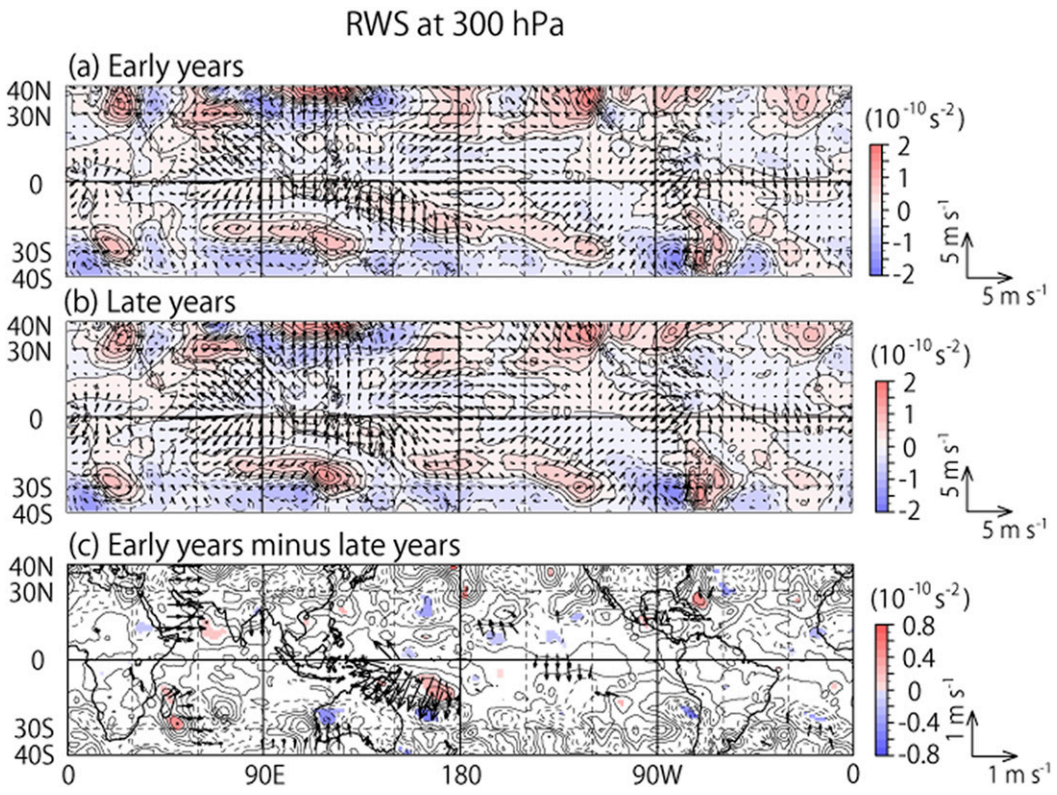

FIG. 10. (a) Early-, (b) late-, and (c) early-minus-late SFW composites of RWS (color) and the horizontal components of divergent wind (arrows) near the tropics at 300 hPa in period 2′. Only areas with the 95% confidence level for a two-sided t test are colored in (c). Arrows whose zonal or meridional component is significant at the 95% confidence level for a two-sided t test are drawn. A reference arrow is given on the right-hand side of each panel.

in the subtropics due to the prominent meridional component of divergent wind at the edge of a region with large divergence and larger absolute vorticity gradient toward higher latitudes. Therefore, large RWS is observed outside the tropics (Shimizu and de Albuquerque Cavalcanti 2011). In the subtropics, significant differences in divergent wind and RWS are observed especially in the SH (Fig. 10c). Near 165°E, significant positive and negative differences in RWS are observed near 15° and 25°S, respectively. A significant difference in southward divergent wind is seen to the northeast of Australia.

c. *Remote responses to tropical heating in a linear barotropic model*

The impact of tropical heating and the background flow on $s = 1$ responses at high latitudes is investigated using a linear barotropic model. We employ a steady barotropic vorticity equation linearized about the streamfunction at 300 hPa (Ting 1996; Ambrizzi and Hoskins 1997; Watanabe 2004):

$$J(\psi_0, \nabla^2\psi_1) + J(\psi_1, \nabla^2\psi_0 + f) + \alpha\nabla^2\psi_1 + \nu\nabla^6\psi_1 = S, \qquad (9)$$

where J denotes the Jacobian operator; ψ_0 and ψ_1 are the background and perturbation streamfunctions, respectively; S is an anomalous vorticity source; α is a linear damping coefficient; and ν is a biharmonic diffusion coefficient. The background streamfunction ψ_0 is calculated from zonal and meridional winds at 300 hPa in the reanalysis data. The perturbation streamfunction ψ_1 is a steady response obtained by solving Eq. (9) with given ψ_0 and S. For S in the linear barotropic model, RWS in the reanalysis data multiplied by a weighting function $f(\phi)$ is used, where $f(\phi) = 1$ for $|\phi| < 30°$; $f(\phi) = 0.5\,\{\cos[18(|\phi| - 30°)] + 1\}$ for $30° < |\phi| < 40°$; and $f(\phi) = 0$ for $|\phi| > 40°$. The coefficient α is set to $(10\ \text{days})^{-1}$. The coefficient ν is determined such as to damp the smallest-scale eddy in 1 day (Watanabe 2004). A horizontal resolution is T21. We use early- and late-SFW composites, and climatology of ψ_0 and S. We denote the kind of ψ_0 and S used in each experiment. For example, an experiment with climatological ψ_0 and an early-SFW composite of S is referred to as $[\psi_0^C, S^E]$, and an experiment with climatological ψ_0 and a late-SFW composite of S is $[\psi_0^C, S^L]$. The impact of S on responses at high latitudes is examined by calculating a difference in responses between a set of two experiments $[\psi_0^C, S^E]$ and $[\psi_0^C, S^L]$. Similarly, the impact of ψ_0 is examined by calculating a difference between $[\psi_0^E, S^C]$ and $[\psi_0^L, S^C]$. In this way, the influences of S and ψ_0 are separately investigated. The analysis is focused on the $s = 1$ component of the difference in responses at high latitudes to explore the larger amplitudes of tropospheric $s = 1$ QSWs in early-SFW years than late-SFW years.

Figure 11 shows differences in $s = 1$ steady responses in period 2′. A large difference in $s = 1$ responses is observed for a

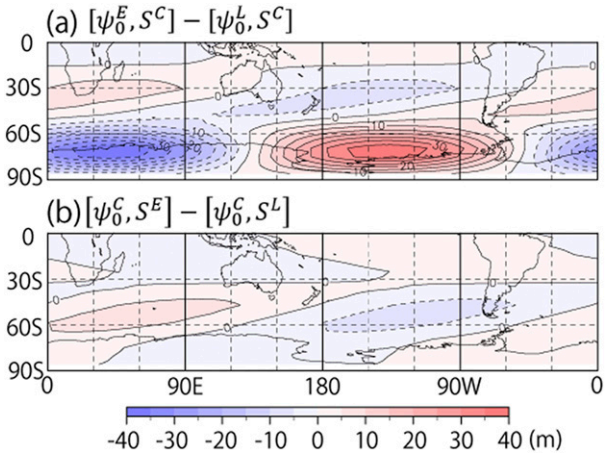

FIG. 11. (a) A difference in $s = 1$ steady responses expressed as GPH between experiments $[\psi_0^E, S^C]$ and $[\psi_0^L, S^C]$ in period 2′. (b) As in (a), but for $[\psi_0^C, S^E]$ and $[\psi_0^C, S^L]$.

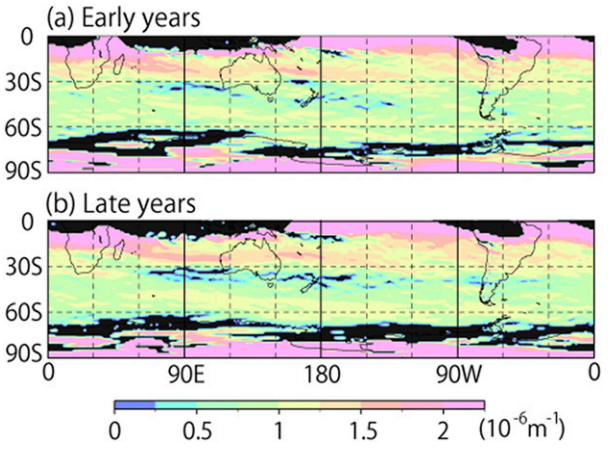

FIG. 12. Total wavenumber for stationary barotropic Rossby waves calculated from (a) early- and (b) late-SFW composites of zonal wind at 300 hPa in period 2′. The total wavenumber is colored black in regions with imaginary K_s.

set of experiments $[\psi_0^E, S^C]$ and $[\psi_0^L, S^C]$ (Fig. 11a). The longitudinal phase structure of the difference in $s = 1$ responses between $[\psi_0^E, S^C]$ and $[\psi_0^L, S^C]$ is similar to that of the difference in $s = 1$ stationary waves in the upper troposphere in the reanalysis data at high latitudes (Figs. 8c and 11a). The magnitude of the difference is comparable to that in $s = 1$ stationary waves. In contrast, a difference between $[\psi_0^C, S^E]$ and $[\psi_0^C, S^L]$ is much smaller than the difference between $[\psi_0^E, S^C]$ and $[\psi_0^L, S^C]$ (Figs. 11a,b). These results suggest that the larger amplitudes of upper tropospheric $s = 1$ QSWs in early-SFW years are attributed to differences in the background flow in period 2′. Note that the results support use of the linear barotropic model to investigate the cause of the difference in amplitudes of tropospheric $s = 1$ QSWs.

5. Discussion

a. *Wave propagation characteristics associated with the background flow*

It is suggested in subsection 4c that the larger amplitudes of $s = 1$ QSWs in the upper troposphere in early-SFW years are attributable to differences in the background flow. In this subsection, the differences in the background flow are examined by comparing wave propagation characteristics associated with the background flow for stationary barotropic Rossby waves in early- and late- SFW years. For this purpose, the total wavenumber for stationary barotropic Rossby waves is used (Hoskins and Karoly 1981; Hoskins and Ambrizzi 1993):

$$K_s = \sqrt{\frac{2\Omega\cos\phi}{a} - \frac{\left[\frac{(u\cos\phi)_\phi}{a^2\cos\phi}\right]_\phi}{u}}. \tag{10}$$

Figure 12 shows K_s in early- and late-SFW years in period 2′. Rossby waveguides, which are areas with large K_s sandwiched by imaginary or small K_s, are seen along the jets in 60°–50°S and 30°–20°S especially in the longitudinal range of 60°E–120°W in both early- and late-SFW years (Figs. 9a,b and 12). For late-SFW years, areas with imaginary or small K_s are also observed near 120°–60°W at midlatitudes (Fig. 12b). There are differences in areas of imaginary or small K_s, where propagation of stationary barotropic Rossby waves is inhibited, at midlatitudes between early- and late-SFW years. The areas of imaginary or small K_s in early-SFW years are blurred compared to those in late-SFW years in the longitudinal range of 60°E–60°W (Fig. 12). This means that it is easier for stationary Rossby waves to propagate latitudinally in this longitudinal range in early-SFW years than late-SFW years.

b. *Quasi-stationary Rossby waves propagating from lower latitudes*

In this subsection, the influence of quasi-stationary Rossby waves propagating from lower latitudes in amplifying $s = 1$ QSWs at high latitudes is discussed. To diagnose propagation of quasi-stationary Rossby waves, the horizontal components of the wave activity flux for quasi-stationary QG eddies derived by Takaya and Nakamura (2001) are used:

$$\frac{\cos\phi}{2\sqrt{[u]^2+[v]^2}}\begin{pmatrix} \frac{[u]}{a^2\cos^2\phi}\left\{\left(\frac{\partial\psi^*}{\partial\lambda}\right)^2 - \psi^*\frac{\partial^2\psi^*}{\partial\lambda^2}\right\} + \frac{[v]}{a^2\cos\phi}\left\{\frac{\partial\psi^*}{\partial\lambda}\frac{\partial\psi^*}{\partial\phi} - \psi^*\frac{\partial^2\psi^*}{\partial\lambda\partial\phi}\right\} \\ \frac{[u]}{a^2\cos\phi}\left\{\frac{\partial\psi^*}{\partial\lambda}\frac{\partial\psi^*}{\partial\phi} - \psi^*\frac{\partial^2\psi^*}{\partial\lambda\partial\phi}\right\} + \frac{[v]}{a^2}\left\{\left(\frac{\partial\psi^*}{\partial\phi}\right)^2 - \psi^*\frac{\partial^2\psi^*}{\partial\phi^2}\right\} \end{pmatrix}, \tag{11}$$

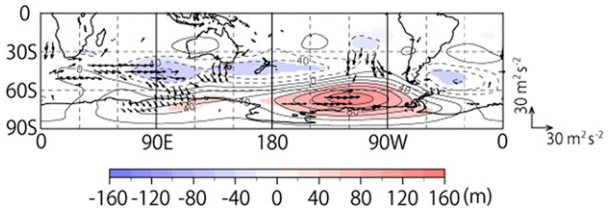

FIG. 13. Early-minus-late SFW composites of GPH (color) and the horizontal components of the wave activity flux for quasi-stationary Rossby waves (arrows) at 300 hPa in period 2′. Only areas with the 95% confidence level for a two-sided t test are colored. Arrows whose zonal or meridional component is significant at the 95% confidence level for a two-sided t test are drawn. A reference arrow is given on the right-hand side of the figure. Arrows are drawn southward of 20°S.

where ψ is the streamfunction; λ is the longitude; and the square brackets and asterisks denote time means and deviations from the time means, respectively. In the present study, mean fields are defined as 60-day low-pass filtered climatology for 38 years, while quasi-stationary eddies are extracted as 15-day low-pass filtered anomalies from the climatological mean fields to adequately eliminate synoptic-scale variations (Kidson 1988). The wave activity flux is parallel to the group velocity of Rossby waves. The wave activity flux is independent of wave phases even if quadratic terms in the formula are not averaged in time for monochromatic waves (Plumb 1985).

Early-minus-late SFW composites of GPH and the horizontal components of the wave activity flux for quasi-stationary Rossby waves at 300 hPa in period 2′ are shown in Fig. 13. Differences in southward wave activity flux are observed in the range of 80°–120°E near 60°S, to the south of Australia, and in the range of 120°–90°W near 40°S. In the longitudinal ranges of 80°–120°E, 130°–150°E, and 120°–90°W, areas of imaginary or small K_s at midlatitudes are blurred in early-SFW years compared to late-SFW years (Fig. 12). Therefore, it is suggested that differences in wave propagation characteristics that arise from the differences in areas of imaginary or small K_s contribute to the differences in southward wave activity flux in these longitudinal ranges.

Significant GPH differences are observed in the longitudinal range of 90°E–90°W southward of 30°S (Fig. 13). Theoretically, the wave activity flux traces centers of GPH anomalies (Takaya and Nakamura 2001). Thus, the correspondence between differences in GPH and the horizontal components of the wave activity flux is examined. In the longitudinal range of 90°–120°E, a significant difference in southward wave activity flux traces from a center of a negative GPH difference to a center of a positive difference (Fig. 13). To the south of Australia, a significant difference in southward wave activity flux apparently corresponds to a negative GPH difference. In the longitudinal range of 120°–90°W, a difference in southward wave activity flux points from a negative GPH difference toward a positive difference near the Amundsen Sea. Therefore, the negative and positive GPH differences in the longitudinal range of 90°E–90°W may be associated with quasi-stationary Rossby waves propagating from lower latitudes.

The significant large positive GPH difference, which may be associated with quasi-stationary Rossby waves propagating from lower latitudes, is observed near the Amundsen Sea (Fig. 13), where the ridge of $s = 1$ stationary waves in early- and late-SFW years is located (Figs. 8a,b). This suggests that Rossby waves propagating from lower latitudes reinforce the ridge of $s = 1$ stationary waves in early-SFW years through constructive interference between them. This feature is reminiscent of remote responses to the canonical El Niño in the Northern Hemisphere polar stratosphere (Domeisen et al. 2019). The weaker polar vortex accompanied by amplification of $s = 1$ stationary waves is observed in the stratosphere during the canonical El Niño. Deepening of the Aleutian low associated with characteristic extratropical teleconnection that closely resembles the Pacific–North American pattern occurs in the troposphere during the canonical El Niño. A trough of the climatological tropospheric $s = 1$ stationary waves is located near the Bering Sea. It is considered that the correspondence between the negative GPH anomalies and the trough of the climatological $s = 1$ stationary waves leads to amplification of $s = 1$ stationary waves in the troposphere, and hence the weaker polar vortex in the stratosphere (Garfinkel and Hartmann 2008; Garfinkel et al. 2010; Hegyi and Deng 2011).

6. Concluding remarks

In this study, the relation between the timing of SFW and tropospheric circulation is explored by comparing early- and late-SFW years. The analysis is focused on $s = 1$ QSWs, whose amplitudes are the largest of SH extratropical planetary waves in both the stratosphere and troposphere and attain a maximum in the austral spring (Randel 1988; Quintanar and Mechoso 1995a; Turner et al. 2017). Our main results are summarized as follows:

- Amplitudes of $s = 1$ QSWs are larger in early-SFW years than late-SFW years in both the stratosphere and troposphere from the late austral winter to spring. Larger upward EP flux due to $s = 1$ QSWs is observed from the troposphere to the stratosphere in early-SFW years. These results indicate that the larger $s = 1$ QSW amplitudes originate in the troposphere.
- Larger EP flux convergence due to $s = 1$ QSWs is observed in the stratosphere in early-SFW years. This likely leads to earlier seasonal evolution of the PNJ, and hence earlier SFWs.
- A comparison of the distribution of the refractive index squared n^2 between early- and late-SFW years reveals more favorable conditions for propagation of $s = 1$ stationary waves into the polar stratosphere in early-SFW years in period 1. The difference in the distribution of n^2 is probably related to the more advanced poleward migration of the PNJ core in early-SFW years than late-SFW years.
- Numerical calculations using a linear barotropic model show that the larger amplitudes of tropospheric $s = 1$ QSWs are attributed to differences in the background flow rather than tropical RWS in the austral spring. It is suggested that the differences in the background flow that affect amplitudes of

$s = 1$ QSWs at high latitudes are related to differences in wave propagation characteristics associated with the structure of the midlatitude jets.

Acknowledgments. We would like to express our gratitude to Hisashi Nakamura, Toshiyuki Hibiya, Keita Iga, and Masahiro Watanabe for their valuable comments and suggestions. We thank Kazuaki Nishii for his constructive comments and instruction in the wave activity flux for quasi-stationary QG eddies. We also thank two anonymous reviewers for their critical reading and constructive comments. The linear barotropic model is provided by Michiya Hayashi and Masahiro Watanabe. All figures in the present study are depicted using Dennou Club Library. We thank Martha Evonuk from Edanz Group (https://en-author-services.edanzgroup.com/ac) for editing a draft of this manuscript. This work was supported by JST CREST Grant JPMJCR1663 and JSPS KAKENHI Grant JP18H01276.

Data availability statement. MERRA-2 data are provided by https://gmao.gsfc.nasa.gov/reanalysis/MERRA-2/data_access/.

REFERENCES

Ambrizzi, T., and B. J. Hoskins, 1997: Stationary Rossby-wave propagation in a baroclinic atmosphere. *Quart. J. Roy. Meteor. Soc.*, **123**, 919–928, https://doi.org/10.1002/qj.49712354007.

——, ——, and H.-H. Hsu, 1995: Rossby wave propagation and teleconnection patterns in the austral winter. *J. Atmos. Sci.*, **52**, 3661–3672, https://doi.org/10.1175/1520-0469(1995)052<3661:RWPATP>2.0.CO;2.

Andrews, D. G., and M. E. McIntyre, 1976: Planetary waves in horizontal and vertical shear: The generalized Eliassen–Palm relation and the mean zonal acceleration. *J. Atmos. Sci.*, **33**, 2031–2048, https://doi.org/10.1175/1520-0469(1976)033<2031:PWIHAV>2.0.CO;2.

——, and ——, 1978: Generalized Eliassen–Palm and Charney–Drazin theorems for waves on axisymmetric mean flows in compressible atmospheres. *J. Atmos. Sci.*, **35**, 175–185, https://doi.org/10.1175/1520-0469(1978)035<0175:GEPACD>2.0.CO;2.

——, J. R. Holton, and C. B. Leovy, 1987: *Middle Atmosphere Dynamics*. Academic Press, 489 pp.

Black, R. X., and B. A. McDaniel, 2007: Interannual variability in the Southern Hemisphere circulation organized by stratospheric final warming events. *J. Atmos. Sci.*, **64**, 2968–2974, https://doi.org/10.1175/JAS3979.1.

Butchart, N., and Coauthors, 2011: Multimodel climate and variability of the stratosphere. *J. Geophys. Res.*, **116**, D05102, https://doi.org/10.1029/2010JD014995.

Butler, A. H., and D. I. V. Domeisen, 2021: The wave geometry of final stratospheric warming events. *Wea. Climate Dyn.*, **2**, 453–474, https://doi.org/10.5194/wcd-2-453-2021.

Byrne, N. J., and T. G. Shepherd, 2018: Seasonal persistence of circulation anomalies in the Southern Hemisphere stratosphere and its implications for the troposphere. *J. Climate*, **31**, 3467–3483, https://doi.org/10.1175/JCLI-D-17-0557.1.

Domeisen, D. I. V., C. I. Garfinkel, and A. H. Butler, 2019: The teleconnection of El Niño Southern Oscillation to the stratosphere. *Rev. Geophys.*, **57**, 5–47, https://doi.org/10.1029/2018RG000596.

Eyring, V., and Coauthors, 2006: Assessment of temperature, trace species, and ozone in chemistry-climate model simulations of the recent past. *J. Geophys. Res.*, **111**, D22308, https://doi.org/10.1029/2006JD007327.

Garfinkel, C. I., and D. L. Hartmann, 2008: Different ENSO teleconnections and their effects on the stratospheric polar vortex. *J. Geophys. Res.*, **113**, D18114, https://doi.org/10.1029/2008JD009920.

——, ——, and F. Sassi, 2010: Tropospheric precursors of anomalous Northern Hemisphere stratospheric polar vortices. *J. Climate*, **23**, 3282–3299, https://doi.org/10.1175/2010JCLI3010.1.

Gelaro, R., and Coauthors, 2017: The Modern-Era Retrospective Analysis for Research and Applications, version 2 (MERRA-2). *J. Climate*, **30**, 5419–5454, https://doi.org/10.1175/JCLI-D-16-0758.1.

Haigh, J. D., and H. K. Roscoe, 2009: The final warming date of the Antarctic polar vortex and influences on its interannual variability. *J. Climate*, **22**, 5809–5819, https://doi.org/10.1175/2009JCLI2865.1.

Harvey, V. L., R. B. Pierce, T. D. Fairlie, and M. H. Hitchman, 2002: A climatology of stratospheric polar vortices and anticyclones. *J. Geophys. Res.*, **107**, 4442, https://doi.org/10.1029/2001JD001471.

Hegyi, B. M., and Y. Deng, 2011: A dynamical fingerprint of tropical Pacific sea surface temperatures on the decadal-scale variability of cool-season Arctic precipitation. *J. Geophys. Res.*, **116**, D20121, https://doi.org/10.1029/2011JD016001.

Hio, Y., and S. Yoden, 2005: Interannual variations of the seasonal march in the Southern Hemisphere stratosphere for 1979–2002 and characterization of the unprecedented year 2002. *J. Atmos. Sci.*, **62**, 567–580, https://doi.org/10.1175/JAS-3333.1.

Hirano, S., M. Kohma, and K. Sato, 2016: A three-dimensional analysis on the role of atmospheric waves in the climatology and interannual variability of stratospheric final warming in the Southern Hemisphere. *J. Geophys. Res. Atmos.*, **121**, 8429–8443, https://doi.org/10.1002/2015JD024481.

Hoskins, B. J., and D. J. Karoly, 1981: The steady linear response of a spherical atmosphere to thermal and orographic forcing. *J. Atmos. Sci.*, **38**, 1179–1196, https://doi.org/10.1175/1520-0469(1981)038<1179:TSLROA>2.0.CO;2.

——, and T. Ambrizzi, 1993: Rossby wave propagation on a realistic longitudinally varying flow. *J. Atmos. Sci.*, **50**, 1661–1671, https://doi.org/10.1175/1520-0469(1993)050<1661:RWPOAR>2.0.CO;2.

Hurwitz, M. M., P. A. Newman, L. D. Oman, and A. M. Molod, 2011: Response of the Antarctic stratosphere to two types of El Niño events. *J. Atmos. Sci.*, **68**, 812–822, https://doi.org/10.1175/2011JAS3606.1.

——, C. I. Garfinkel, P. A. Newman, and L. D. Oman, 2013: Sensitivity of the atmospheric response to warm pool El Niño events to modeled SSTs and future climate forcings. *J. Geophys. Res. Atmos.*, **118**, 13 371–13 382, https://doi.org/10.1002/2013JD021051.

Inatsu, M., and B. J. Hoskins, 2004: The zonal asymmetry of the Southern Hemisphere winter storm track. *J. Climate*, **17**, 4882–4892, https://doi.org/10.1175/JCLI-3232.1.

Jin, D., and B. P. Kirtman, 2009: Why the Southern Hemisphere ENSO responses lead ENSO. *J. Geophys. Res.*, **114**, D23101, https://doi.org/10.1029/2009JD012657.

——, and ——, 2010: How the annual cycle affects the extratropical response to ENSO. *J. Geophys. Res.*, **115**, D06102, https://doi.org/10.1029/2009JD012660.

Karpetchko, A. Y., E. Kyrö, and B. M. Knudsen, 2005: Arctic and Antarctic polar vortices 1957–2002 as seen from the ERA-40 reanalyses. *J. Geophys. Res.*, **110**, D21109, https://doi.org/10.1029/2005JD006113.

Kidson, J. W., 1988: Indices of the Southern Hemisphere zonal wind. *J. Climate*, **1**, 183–194, https://doi.org/10.1175/1520-0442(1988)001<0183:IOTSHZ>2.0.CO;2.

Kinoshita, T., and K. Sato, 2013: A formulation of three-dimensional residual-mean flow applicable both to inertia-gravity waves and to Rossby waves. *J. Atmos. Sci.*, **70**, 1577–1602, https://doi.org/10.1175/JAS-D-12-0137.1.

Langematz, U., and M. Kunze, 2006: An update on dynamical changes in the Arctic and Antarctic stratospheric polar vortices. *Climate Dyn.*, **27**, 647–660, https://doi.org/10.1007/s00382-006-0156-2.

Li, X., E. P. Gerber, D. M. Holland, and C. Yoo, 2015: A Rossby wave bridge from the tropical Atlantic to West Antarctica. *J. Climate*, **28**, 2256–2273, https://doi.org/10.1175/JCLI-D-14-00450.1.

Lim, E.-P., H. H. Hendon, and D. W. J. Thompson, 2018: Seasonal evolution of stratosphere–troposphere coupling in the Southern Hemisphere and implications for the predictability of surface climate. *J. Geophys. Res. Atmos.*, **123**, 12 002–12 016, https://doi.org/10.1029/2018JD029321.

Lin, P., Q. Fu, and D. L. Hartmann, 2012: Impact of tropical SST on stratospheric planetary waves in the Southern Hemisphere. *J. Climate*, **25**, 5030–5046, https://doi.org/10.1175/JCLI-D-11-00378.1.

McLandress, C., T. G. Shepherd, S. Polavarapu, and S. R. Beagley, 2012: Is missing orographic gravity wave drag near 60°S the cause of the stratospheric zonal wind biases in chemistry–climate models? *J. Atmos. Sci.*, **69**, 802–818, https://doi.org/10.1175/JAS-D-11-0159.1.

Newman, P. A., E. R. Nash, S. R. Kawa, S. A. Montzka, and S. M. Schauffler, 2006: When will the Antarctic ozone hole recover? *Geophys. Res. Lett.*, **33**, L12814, https://doi.org/10.1029/2005GL025232.

Plumb, R. A., 1985: On the three-dimensional propagation of stationary waves. *J. Atmos. Sci.*, **42**, 217–229, https://doi.org/10.1175/1520-0469(1985)042<0217:OTTDPO>2.0.CO;2.

Quintanar, A. I., and C. R. Mechoso, 1995a: Quasi-stationary waves in the Southern Hemisphere. Part I: Observational data. *J. Climate*, **8**, 2659–2672, https://doi.org/10.1175/1520-0442(1995)008<2659:QSWITS>2.0.CO;2.

——, and ——, 1995b: Quasi-stationary waves in the Southern Hemisphere. Part II: Generation mechanisms. *J. Climate*, **8**, 2673–2690, https://doi.org/10.1175/1520-0442(1995)008<2673:QSWITS>2.0.CO;2.

Randel, W. J., 1988: The seasonal evolution of planetary waves in the Southern Hemisphere stratosphere and troposphere. *Quart. J. Roy. Meteor. Soc.*, **114**, 1385–1409, https://doi.org/10.1002/qj.49711448403.

Salby, M. L., E. A. Titova, and L. Deschamps, 2012: Changes of the Antarctic ozone hole: Controlling mechanisms, seasonal predictability, and evolution. *J. Geophys. Res.*, **117**, D10111, https://doi.org/10.1029/2011JD016285.

Sardeshmukh, P. D., and B. J. Hoskins, 1988: The generation of global rotational flow by steady idealized tropical divergence. *J. Atmos. Sci.*, **45**, 1228–1251, https://doi.org/10.1175/1520-0469(1988)045<1228:TGOGRF>2.0.CO;2.

Schneider, D. P., Y. Okumura, and C. Deser, 2012: Observed Antarctic interannual climate variability and tropical linkages. *J. Climate*, **25**, 4048–4066, https://doi.org/10.1175/JCLI-D-11-00273.1.

Shimizu, M. H., and I. F. de Albuquerque Cavalcanti, 2011: Variability patterns of Rossby wave source. *Climate Dyn.*, **37**, 441–454, https://doi.org/10.1007/s00382-010-0841-z.

Sun, L., and W. A. Robinson, 2009: Downward influence of stratospheric final warming events in an idealized model. *Geophys. Res. Lett.*, **36**, L03819, https://doi.org/10.1029/2008GL036624.

——, ——, and G. Chen, 2011: The role of planetary waves in the downward influence of stratospheric final warming events. *J. Atmos. Sci.*, **68**, 2826–2843, https://doi.org/10.1175/JAS-D-11-014.1.

Takaya, K., and H. Nakamura, 2001: A formulation of a phase independent wave-activity flux for stationary and migratory quasigeostrophic eddies on a zonally varying basic flow. *J. Atmos. Sci.*, **58**, 608–627, https://doi.org/10.1175/1520-0469(2001)058<0608:AFOAPI>2.0.CO;2.

Ting, M., 1996: Steady linear response to tropical heating in barotropic and baroclinic models. *J. Atmos. Sci.*, **53**, 1698–1709, https://doi.org/10.1175/1520-0469(1996)053<1698:SLRTTH>2.0.CO;2.

Turner, J., J. S. Hosking, T. J. Bracegirdle, T. Phillips, and G. J. Marshall, 2017: Variability and trends in the Southern Hemisphere high latitude, quasi-stationary planetary waves. *Int. J. Climatol.*, **37**, 2325–2336, https://doi.org/10.1002/joc.4848.

Watanabe, M., 2004: Asian jet waveguide and a downstream extension of the North Atlantic Oscillation. *J. Climate*, **17**, 4674–4691, https://doi.org/10.1175/JCLI-3228.1.

Waugh, D. W., W. J. Randel, S. Pawson, P. A. Newman, and E. R. Nash, 1999: Persistence of the lower stratospheric polar vortices. *J. Geophys. Res.*, **104**, 27 191–27 201, https://doi.org/10.1029/1999JD900795.

Wilcox, L. J., and A. J. Charlton-Perez, 2013: Final warming of the Southern Hemisphere polar vortex in high- and low-top CMIP5 models. *J. Geophys. Res. Atmos.*, **118**, 2535–2546, https://doi.org/10.1002/jgrd.50254.

Yang, E.-S., D. M. Cunnold, M. J. Newchurch, R. J. Salawitch, M. P. McCormick, J. M. Russell III, J. M. Zawodny, and S. J. Oltmans, 2008: First stage of Antarctic ozone recovery. *J. Geophys. Res.*, **113**, D20308, https://doi.org/10.1029/2007JD009675.

Yuan, X., M. R. Kaplan, and M. A. Cane, 2018: The interconnected global climate system—A review of tropical–polar teleconnections. *J. Climate*, **31**, 5765–5792, https://doi.org/10.1175/JCLI-D-16-0637.1.

Zhou, S. T., M. E. Gelman, A. J. Miller, and J. P. McCormack, 2000: An inter-hemisphere comparison of the persistent stratospheric polar vortex. *Geophys. Res. Lett.*, **27**, 1123–1126, https://doi.org/10.1029/1999GL011018.